JOURNAL OF MATERIALS SCIENCE **36** (2001) 5683–5696

Imaging of surface strain and polishing artefacts in fused silica by environmental scanning electron microscopy

S. P. GALVIN*,§, B. J. GRIFFIN‡, J. BROWNE‡
*Special Research Centre for Advanced Materials and Minerals Processing,
‡Centre for Microscopy and Microanalysis, The University of Western Australia,
Nedlands, W.A. 6907, Australia
E-mail: spgalvin@cyllene.uwa.edu.au

The recently developed application of charge contrast imaging (CCI), available in variable pressure or environmental scanning electron microscopes (ESEM), has been found to provide images of near surface strain around micro-indentations in fused silica glass. Results suggest this strain contrast information is derived from within a few nanometres of the material surface, making CCI an invaluable tool for the study of nanometre scale surface deformation. Images of indentation strain have also been imaged using backscattered electron (BSE) imaging. The CCI technique has also been applied to the study of fused silica surfaces polished by chemically active polishing abrasives. In the samples studied, CCI provides unique images of linear defects residing below layers of chemically adhered polishing compound. Visualisation of surface strain on sub-nm rms glasses provides supporting evidence for plastic (permanent) deformation of the glass surface at the nanometre level during polishing with certain abrasives and for chemical interactions between the polishing abrasive and glass surface.

1. Introduction

Conventional high vacuum scanning electron microscopy (SEM) traditionally proves to be the most commonly utilised analytical tool for collection of near-surface morphological data through secondary electron (SE) imaging, while chemical information is collected through backscattered electron (BSE) detection. The electron beam sample interactions giving rise to these signals are now well understood [1, 2]. In SE imaging, nanometre scale lateral resolution of surface detail is achievable using modern high brightness field emission sources and low beam energies. These sources result in reduced electron beam interaction volumes within the samples resulting in enhanced lateral resolution and improved surface sensitivity [2]. As an example of high resolution imaging, Postek and Evans [3] were able to identify surface machining defects on diamond tools with vertical amplitudes of less than 10 nm by using low accelerating voltages on uncoated diamond samples.

Unfortunately for optical quality surfaces such as polished glass and thin film silica dielectric layers, the surface amplitudes are smaller still, typically around 1 nm peak-to-valley and cannot be visualised using even high resolution field emission sources. Depth resolutions in SEM's of several nanometres through multi-detector arrays and computer processing have been reported, but these are not widely employed [4]. Furthermore, using backscattered electron detection compositional variations are detectable only at greatly reduced resolutions when compared with secondary electron detection due to sub-surface electron scattering effects [2].

Recently, unusual contrasts on a range of poorly conducting samples have been reported while imaging using variable pressure scanning electron microscopes (VPSEM) or environmental SEM's (ESEM). Termed 'charge contrast imaging' (CCI), this application of ESEM has provided highly resolved and surface specific images of growth zones in gibbsite [5], textural information on alumina [6] and nanometre thick solvent residues on silicon [7]. While this imaging process is complex and as yet not well understood [8], it is believed that a balance between the electron beam, the sample and positive ion gas flood from the electron-gas interaction results in a suppression of all but very near surface electron emissions from the sample. The density of trapped charge at the near-surface becomes the dominant control of image contrast [6]. In the case of gibbsite, these contrasts have been empirically correlated with defect distributions in the material studied [9]. Interestingly, these images have been obtained at high electron accelerating voltages (30 kV) where

§Author to whom all correspondence should be addressed.

classic secondary electron processes should not give rise to such surface specific information.

This paper reports on the newly recognised aspects of CCI in the study of glass surfaces and its practical application in terms of developing a better understanding of microscopic and nano-scale mechanical processes.

2. Experimental procedure

Fused silica samples (code 7940, Corning) were ground and pre-polished to remove sub-surface grinding damage prior to any polishing procedures. Polishing tests employed commercial alumina (Alox, Ferro Corp.) and cerium dioxide (424 K, Ferro Corp.; Siemi Ceria, Siemi Chemicals) abrasives. Indentation test were performed in air using a microhardness tester (Leco) using Vickers and Knoop diamond indenters, with loads varying from 5 g to 1 kg and dwell times of 15 seconds.

Specimens were examined in either carbon coated or uncoated conditions using an Electroscan E-3 ESEM or a FEI XL30 ESEM. Imaging was performed in 'wet' mode with water vapour as the chamber gas. Secondary electron signal collection utilised the positively biased 'Griffin' type gaseous electron detector [10] in the Electroscan instrument or the patented large field device (LFD) of FEI in the XL30, typically operating at a positive bias of 500 V. Observations were also performed under high vacuum conditions using the standard Everhart-Thornley type secondary electron detectors. A conventional ESEM low-kV solid state backscattered electron detector was used for BSE imaging. An accelerating voltage of 30 kV was used and working distances of 6–12 mm. Other parameters such as beam current, chamber pressure etc. were varied to optimise image contrasts. The precise operating conditions giving rise to the imaging effects will be discussed below, or for further reference the reader is referred to the paper by Griffin [6].

Comparison of the glass surfaces were made using atomic force microscopy (AFM) (Dimension^{TM} 3000, Digital Instruments). Additionally comparisons were made using a JEOL 6400 SEM, operated at 30 kV and equipped with a standard JEOL solid state BSE detector or, alternatively using a JEOL 6300F field emission SEM (FESEM) operated at 3 kV. Both techniques were employed after coating the sample with a 20 nm evaporated carbon film.

3. Results and discussion

3.1. Indents

3.1.1. Unpolished indentations

Fig. 1 is a conventional secondary electron FESEM image of a 300 gram Vickers indent in polished fused

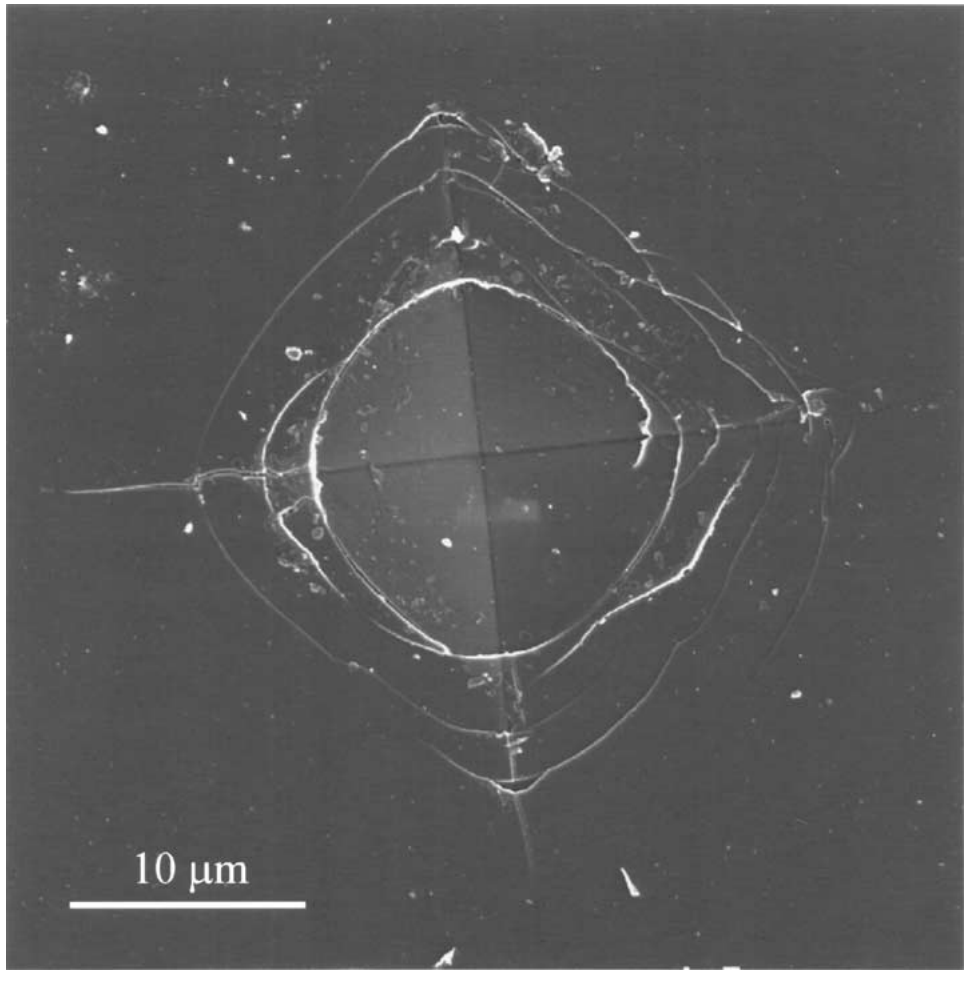

Figure 1 A secondary electron image of a 300 gram load Vickers indent in fused silica obtained at 3 kV with a JEOL 6300F FESEM on a carbon coated specimen. The uniformity of contrast, edge highlighting at cracks, and dark indentation diagonals provides a good example of a conventional secondary electron image.

silica. The image reveals the formation of a permanent residual or 'plastic' pyramidal imprint, absent of any pile-up of displaced material around the periphery of the indenter imprint. Fracturing is noted, with the formation of a series of incomplete ring cracks which are approximately concentric about the load axis of the indent, as well as some radial cracks originating from the indentation corners. These observations are consistent with previous reports of indentation deformation and fracture in fused silica [11–13].

In terms of image characteristics, edge highlighting at the fracture edges are observed, with reduced SE signal intensity at the indentation diagonals. The image exhibits a uniformity of grey levels across the sample, generally absent of strong variations in SEII (Z dependent) derived contrast. This is primarily due to the strong chemical homogeneity and single phase of the fused silica. The left faces of the indenter imprint also exhibit higher brightness those to the right faces of the image, which is attributable to the contribution of some backscattered electrons with appropriate emergence directions on the SE signal collected by the Everhart-Thornley detector. All these features are characteristic of imaging using conventional secondary electron imaging techniques [1].

Fig. 2a–c show similar indentations when imaged uncoated in the Electroscan ESEM at low chamber pressures. Features of the image are qualitatively similar to those obtained with field emission SEM and include an overall uniformity of grey scale and significant edge highlighting effects at fracture sights. Degraded resolution is noted compared with Fig. 1 and is attributed to both the larger electron gun emission source, as well as electron skirt effects due to electron-gas scattering effects [14].

On reducing electron dose rate or fluence, a progressive enhancement of secondary contrast associated with the indent is observed which is not consistent with typically secondary electron imaging characteristics (Fig. 2b and c). Dark diffuse regions appear at the corners of the indentation imprint and are particularly pronounced around the ring crack immediately adjacent to the deformation. Towards the axis of the indentation, these contrasts become more diffuse. Edge highlighting effects at cracks are slightly enhanced by the adjustment in the scan rate.

On reducing fluence further, diminishing contrast of the indentation diagonals is observed to the point where they are barely apparent, while contrast intensifies at the corners of the indentation extending radially

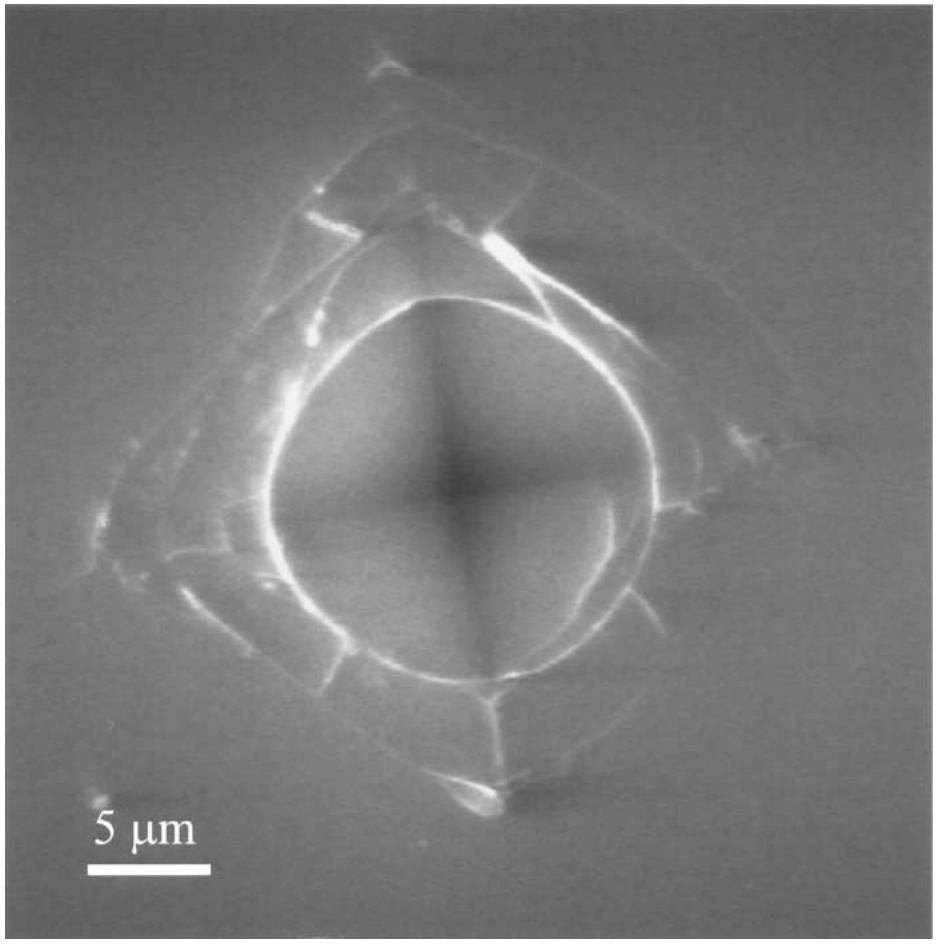

(a)

Figure 2 'SE' (CCI) images showing the progressive development of contrast information around a Vickers indentation in fused silica as the sample imaging conditions are changed. Note the development of strong dark contrasts at the corners of the indentation and the appearance of surface contamination. The image was obtained in the Electroscan E-3 ESEM on an uncoated sample. Images collected at 30 kV using water vapour at a pressure of 1.3 Torr, working distance = 12 mm and scan rate (a) 17 sec/frame, (b) 8.6 sec/frame and (c) 4.3 sec/frame. Images integrated over 16 scans. (*Continued*)

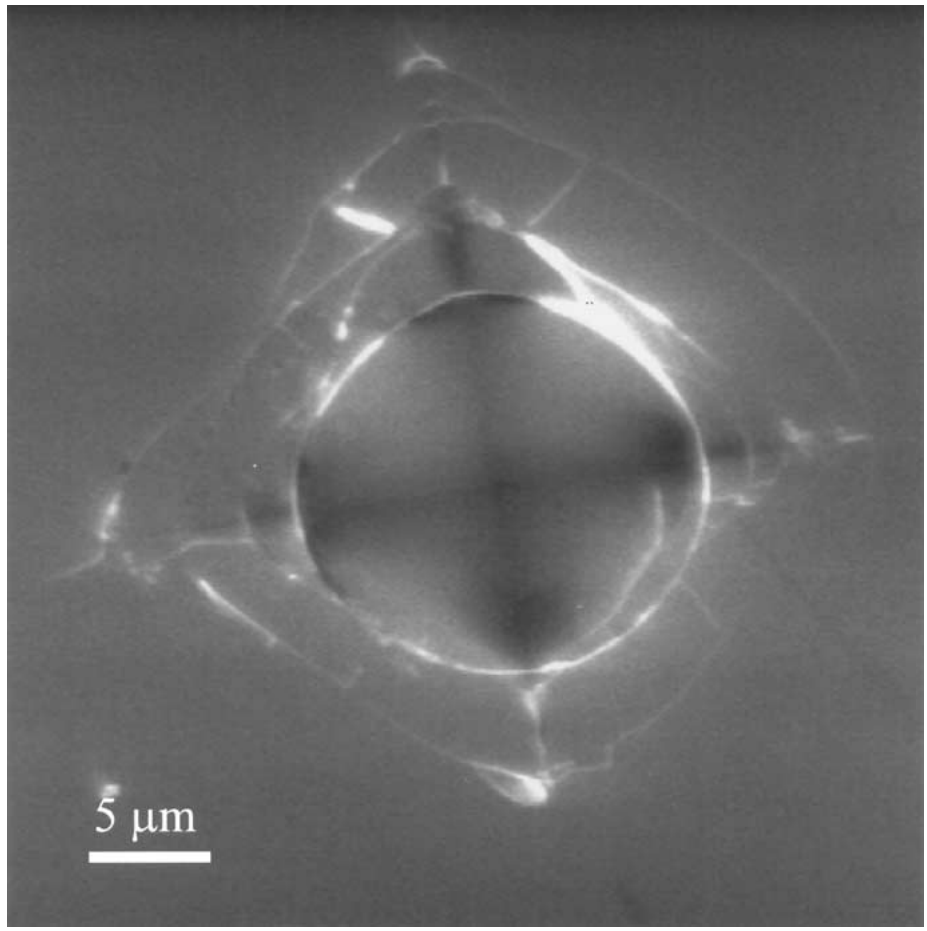

(b)

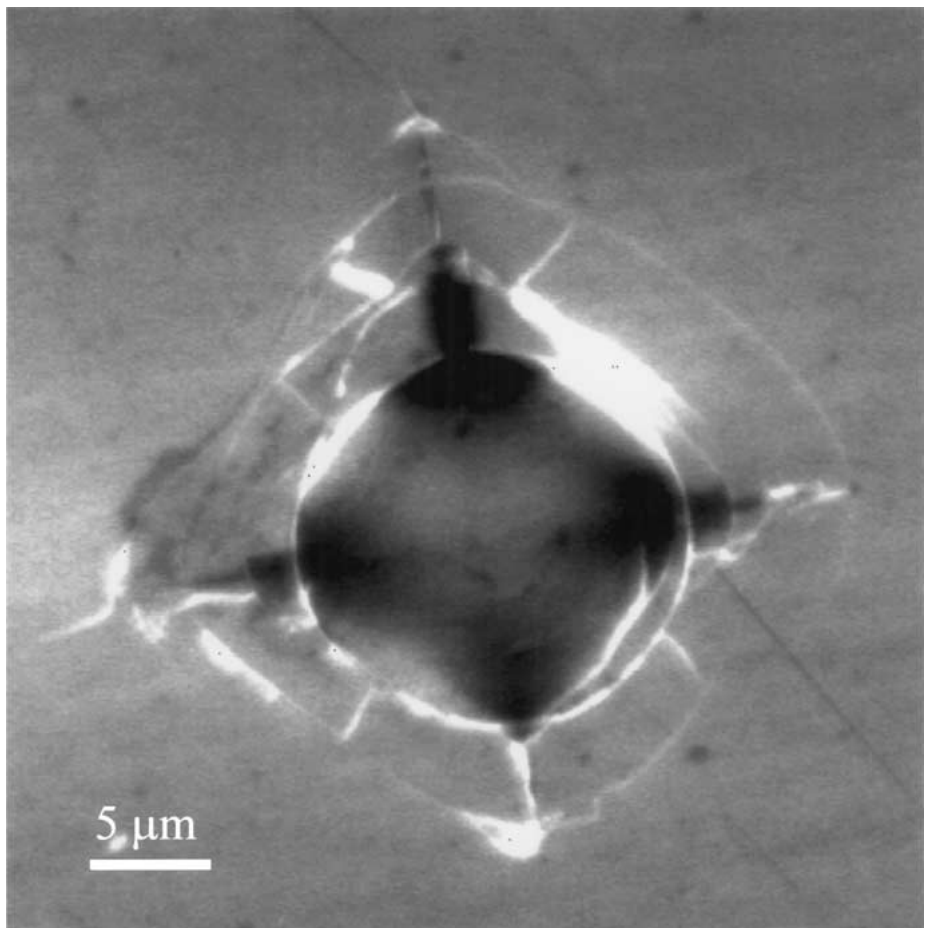

(c)

Figure 2 (*Continued*).

outward along the indentation diagonals (Fig. 2c). In the surrounding undisturbed areas of the specimen contaminant residues arising from atmospheric contact and handling of the specimen have become apparent. These appear as randomly distributed sub-micron stains over the surface. The surface deposits were found to be readily removed using high quality absolute ethanol followed by dry nitrogen blowing.

An AFM image displaying the three dimensional topography of a segment of a Vickers indentation is shown in Fig. 3 for comparison with the previous figures.

Multiple fracture events about the indentation corner are observed, resulting in stepped features generated by the intersection of radial cracks and adjacent cone crack events. The surface topography suggests that during the indentation process the formation of ring cracks and subsidence of the sample under the indenter may lead to inhomogeneous pressure distributions between the face of the diamond indenter and fractured material at the indentation corners. Yielding of this material and localised residual strain development through densification is anticipated at these sites. Fig. 3 suggests the possibility that ESEM image contrast observed in Fig. 2c may be associated with the development of strain.

3.1.2. Sub-indent contrasts

To confirm that the observed image contrasts were independent of surface topography and were associated with strain, samples were progressively polished to remove the indenter imprints and immediately imaged at the same location. Fig. 4 shows that strong contrast is imaged between the deformed material below the indentation site and surrounding non-densified material and is indicative of suppression of electron signal within the deformed zones. The association of contrast information and strain was confirmed by assessing the shape and lateral dimensions of the observed contrast zones and correlating this with surface topography measured by AFM, after the indented-then polished samples had been allowed to anelastically recover over a period of two weeks. Recovered zones appeared as mounds extending up to 50 nm above the reference polished surface and exhibited lateral dimensions consistent with the dimensions of zones detected using ESEM. Anelastic recovery of densified silica under ambient conditions is well established [15, 16].

Measurements on samples indented with Vickers and Knoop indenters have revealed that observed zones strongly reflect the symmetry of the indenter.

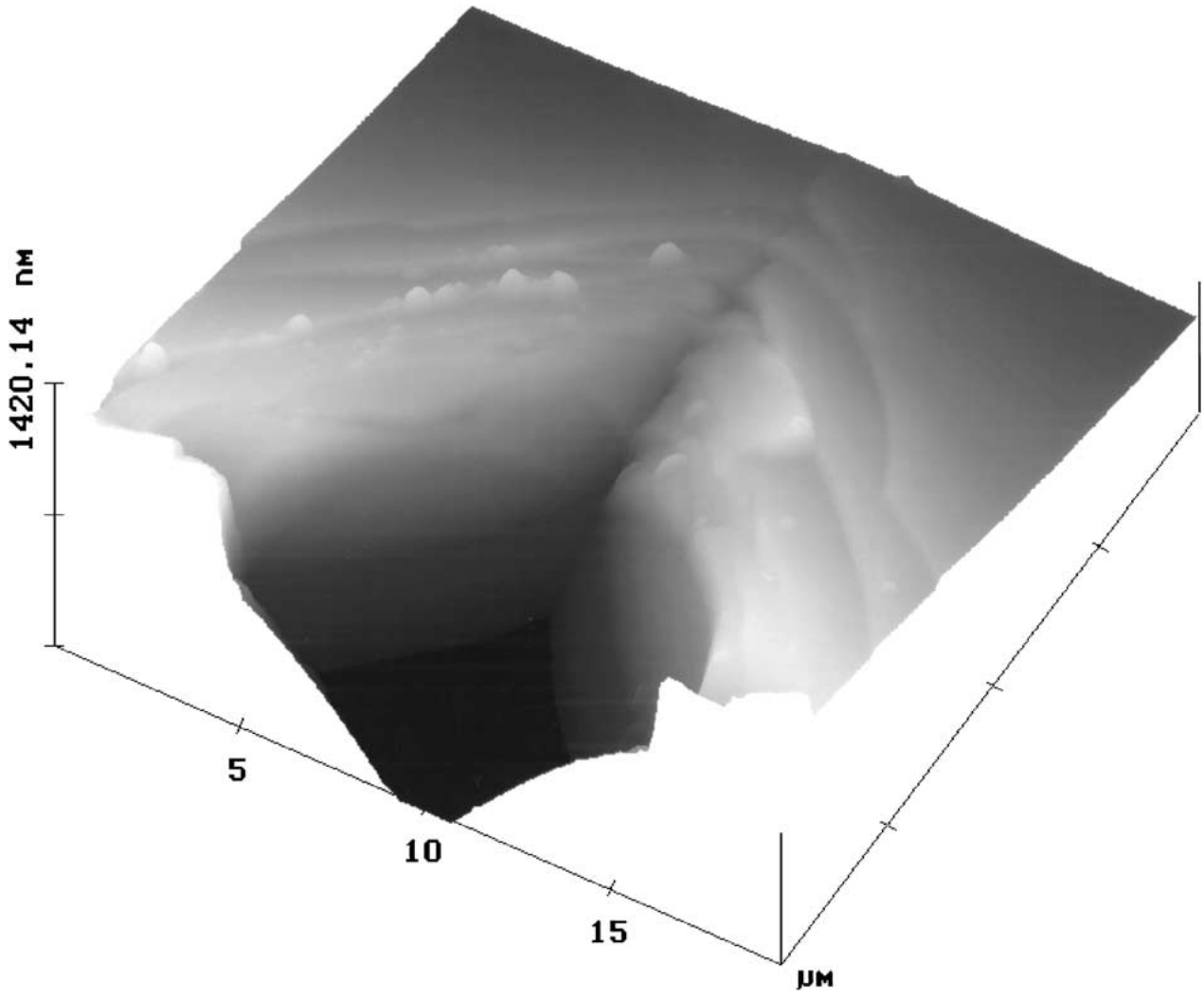

Figure 3 A 20 μm intermittent contact AFM scan of a section of a Vickers indentation in fused silica. Note the absence of pile-up, the formation of concentric ring cracks and the high compaction of material at the corners of the indentation.

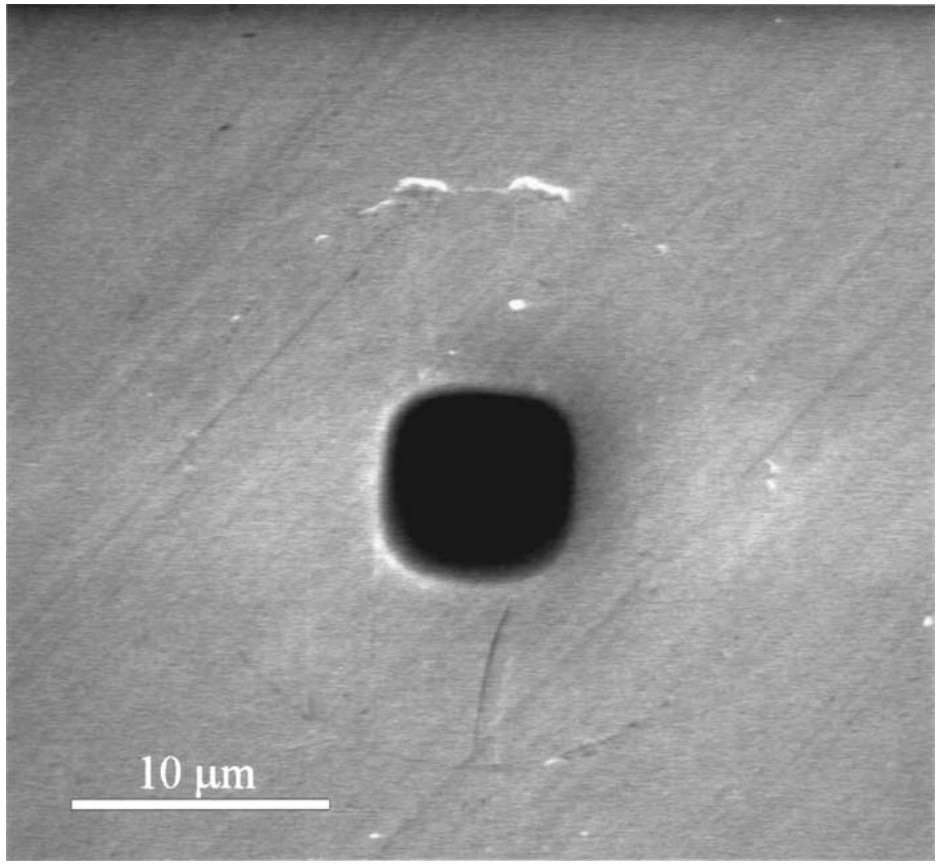

(a)

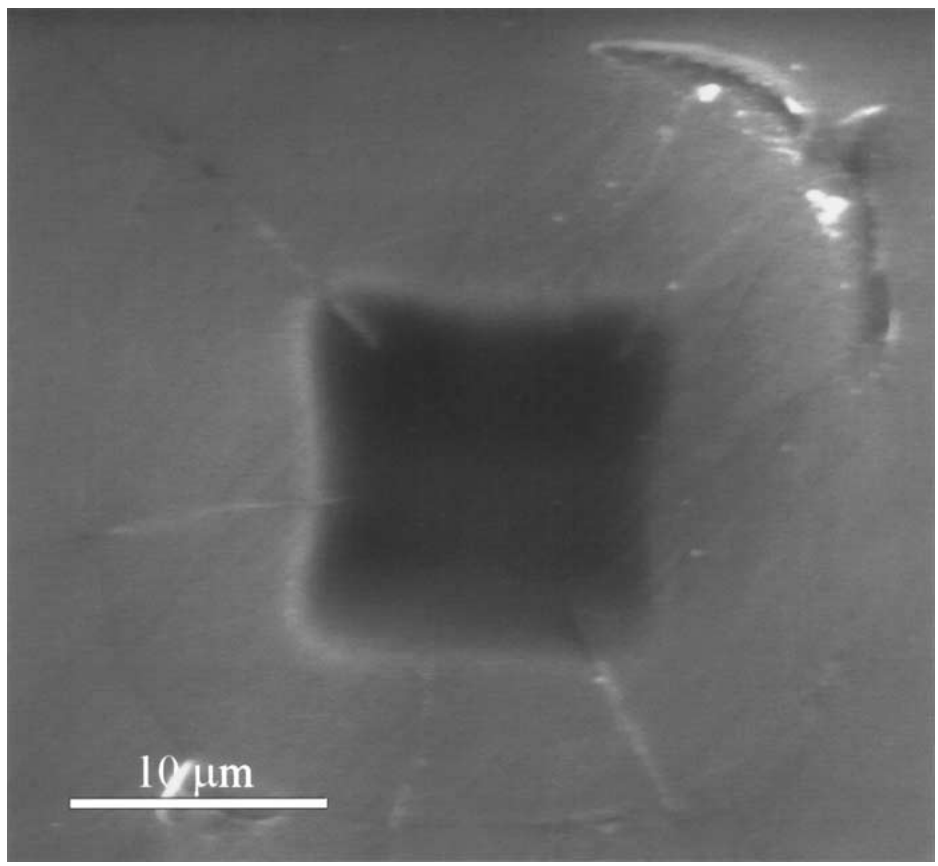

(b)

Figure 4 A CCI image of sub-indent strains after polishing out the residual indenter imprint. Images obtained in the FEI XL30 ESEM ($E = 30$ kV, spot size = 5, $P = 0.4$ Torr and WD = 9.3 mm). (a) a CCI image of a square deformation zone below a 50 gram load Vickers indent, (b) a CCI image shows the deformation zone displays lateral contraction of the zone edges (200 gram load), (c) a CCI image displaying a circular deformation zone suggestive of a more hertzian indentation (25 gram load), (d) the corresponding BSE image to Fig. 4b—the deformation zone appears square owing to the greater depths from which backscattered electron emissions are derived, (e) a CCI image displaying 'normal' CCI contrast conditions (100 gram load), and (f) the corresponding image to Fig. 4e, displaying reversal of the CCI contrast, achieved by lowering the chamber pressure to 0.2 Torr. (*Continued*)

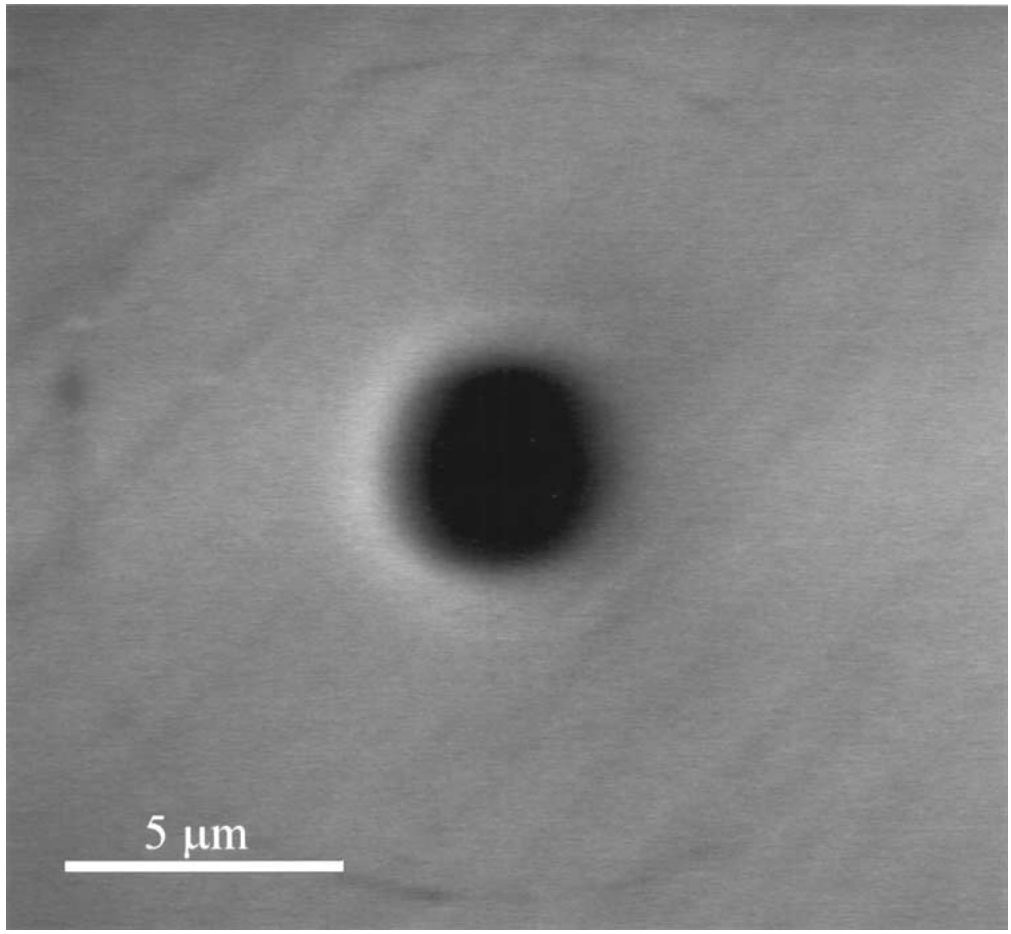

(c)

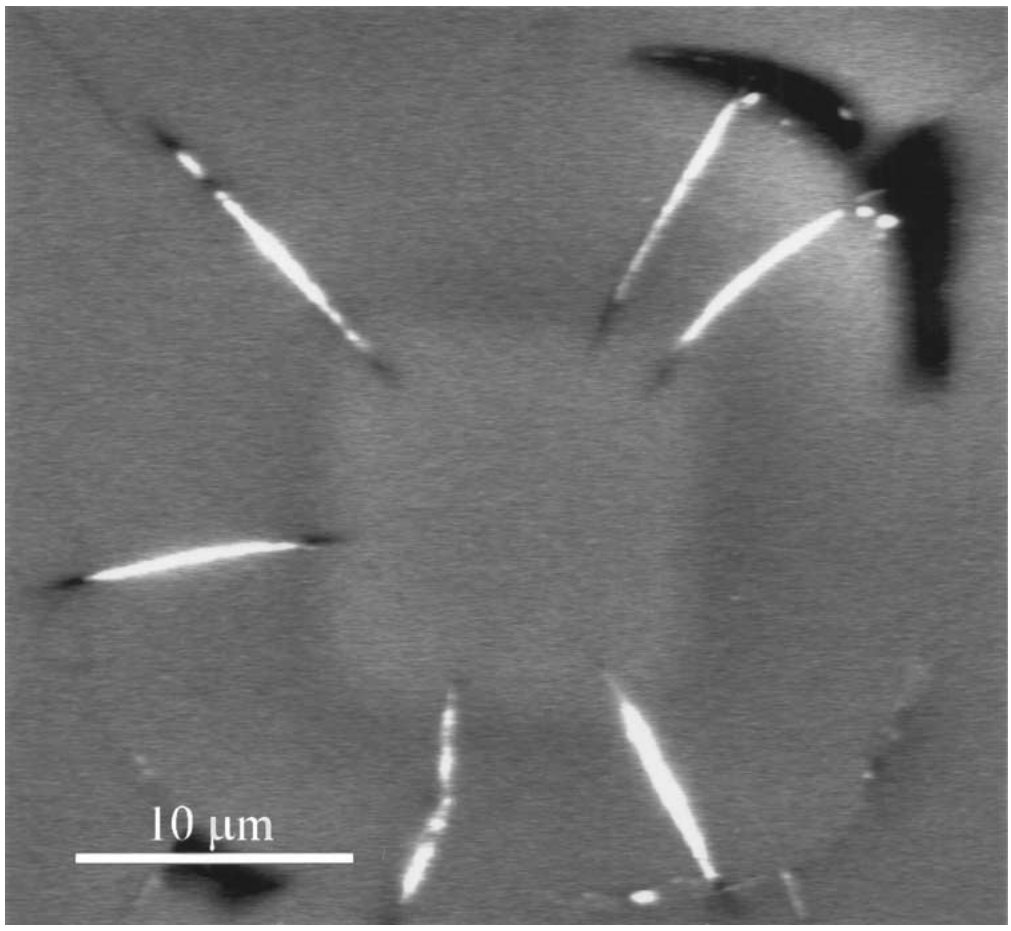

(d)

Figure 4 (*Continued*).

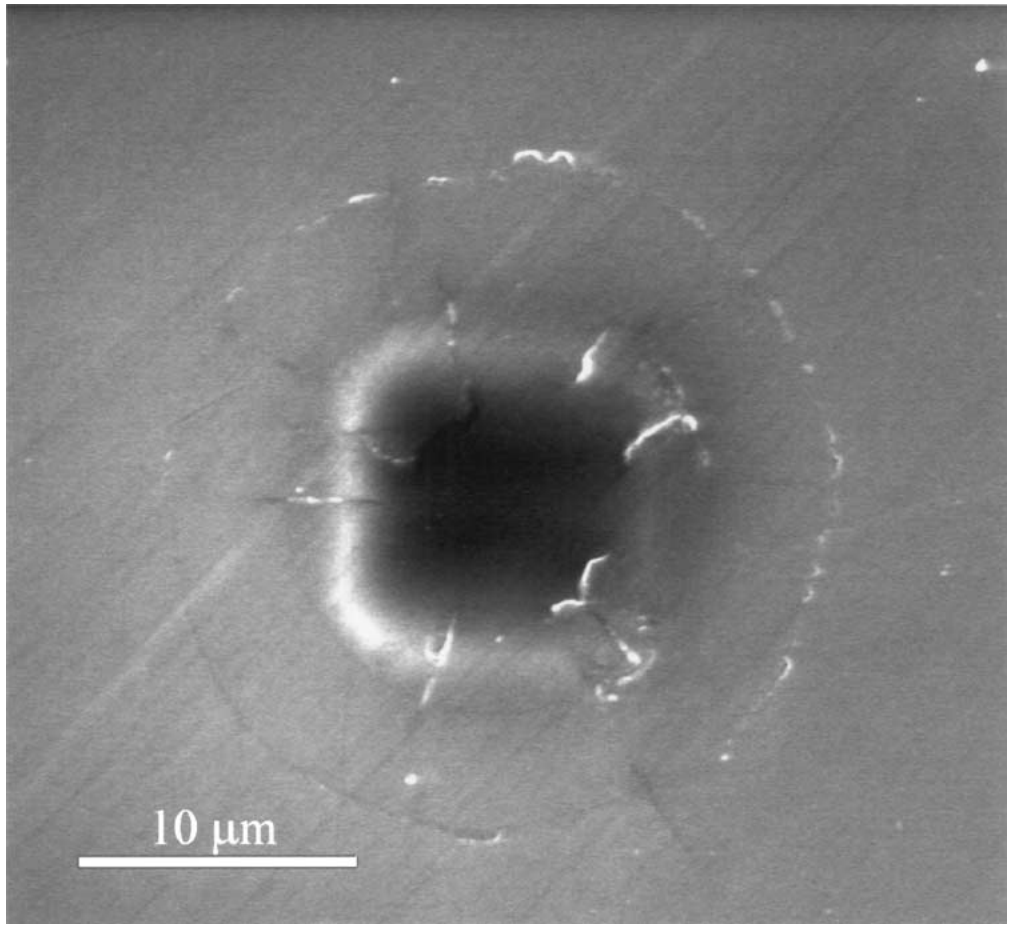

(e)

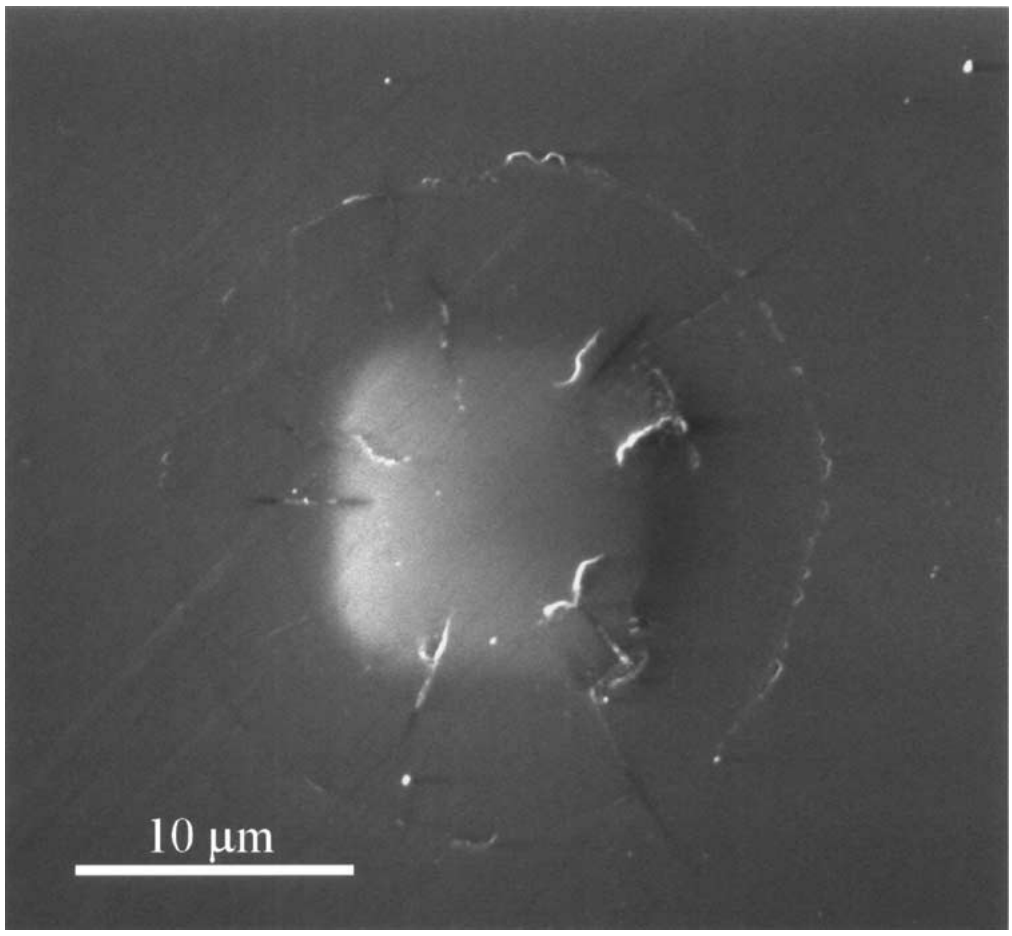

(f)

Figure 4 (*Continued*).

Square geometries, generally with radius corners were observed for Vickers indentations (Fig. 4a), while elongated diamond-shaped zones are associated with Knoop indentations. In some instances lateral contraction of the edges of the post-polished deformation zones were observed (Fig. 4b), suggesting some lateral elastic recovery of the indent volume upon removal of the imposed compressive loads. The extent of elastic contraction was observed qualitatively to be a function of the position of the newly polished surface relative to the original indented surface. Spherical contacts shown in Fig. 4c have also been noted, particularly for low load indentations (10–25 grams load). The shape of these deformation zones appears to be reflective of the deviation of the indenter from the idealised indenter shape and the spherical contact is attributed to the finite radius of the indenter tip leading to a more hertzian deformation zone.

On coating the samples with carbon, all atypical 'SE' contrasts vanished and imaging reverted to more conventional SE imaging characteristics (eg. Fig. 2a). However, backscattered electron contrasts associated with indentations have been imaged in the XL30 operating at low vacuum on uncoated samples, as well as in high vacuum mode after the sample has been coated. Interestingly, BSE contrast is not apparent when using SEM's where the BSE detectors have poor sensitivity to low-energy BSE's compared with typical ESEM BSE detectors (such as in the high vacuum JEOL 6400 SEM) [14]. Fig. 4d shows a BSE image which is the companion to the 'SE' image shown in Fig. 4b. Image contrast of the deformation zones is reversed compared with the 'SE' contrasts and the deformation zone appears characteristically bright. Noticeable degradation in signal to noise and lateral resolution is also apparent in this detection mode compared with 'SE' imaging.

There is excellent correspondence in terms of size of the deformed regions measured using the 'SE' and BSE techniques, although differences in geometry of the contrasts generated by the two techniques are observed. The 'SE' image in Fig. 4b demonstrates some slight lateral recovery of the indented volume while the BSE image displays parallel edges. This difference we attribute to the larger interaction volume from which the BSE signal is derived (owing to the greater energy of the detected electrons) and hence the larger depths from which composite strain information is obtained. Sub-surface fractures revealed after the polishing treatment appear dark in BSE images, except where polishing compound has been incorporated into the fissures as observed in the radial cracks in Fig. 4d. This is attributable to the higher backscattering coefficient of cerium dioxide compared with silica [1, 2, 17].

By manipulating the operating conditions within the ESEM chamber, reversal of the 'SE' image can also be obtained. Fig. 4f shows reversal of the 'SE' image shown in Fig. 4e, produced by dropping the chamber pressure from 0.4 to 0.2 Torr in the XL30, while maintaining all other conditions constant. While the image in many regards appears similar to a BSE image, the information retains its enhanced surface specific characteristic of the 'SE' mode.

3.1.3. Nature of the electron contrasts

The strain contrast information we have observed using 'secondary electron' detection in the ESEM displays characteristics similar to prior reports of charge contrasts imaging (CCI) of gibbsite [5, 6, 18]. In keeping with previously published terminology, the secondary electron images displaying this unusual contrast information are also classified as CCI images.

Characteristic of the observed emissions from fused silica, is a strong suppression of electron signal from within strained regions, the extent to which it shows dependence on the dose of the incident electron beam. Levels of beam dose necessary to provide strongly contrasting CCI are found to be strictly material and microscope dependent. Typically a non-monotonic relationship between beam dose and contrast intensity has been observed. When imaging using the FEI XL30 ESEM, the CCI contrasts on silica were enhanced with an increase in electron beam dose at the sample surface, while contrary trends were noted for the Electroscan E-3 ESEM.

The simplest method found for optimising the acquired signal for normal and CCI imaging conditions is through adjustment in either magnification or scan rate. The images presented here have been firstly optimised for CCI conditions using other variables such as spot size, chamber pressure and bias voltage while scan rate and magnification have been used for dynamic control over the transition between CCI and more conventional SE imaging conditions. These contrasts, however, have shown to be conditional on the sample not being subjected to charge implantation. Excessive beam dose can lead to localised semi-permanent charge implantation which can permanently swamp the subtle CCI information.

The mechanisms behind the variations in the distribution and intensity of the CCI strain contrasts in fused silica are not yet completely understood. The variations, both in terms of spatial distribution and apparent intensity of the strain information with variations in operating conditions, may be interpreted as a change in the sensitivity of the imaging system to surface strains. Alternatively, it may be assumed that the information we obtain from these images simply reflects a greater or lesser depth profiling of the surface strains. Monte carlos simulations on contaminant deposits on silicon have shown that CCI signals are derived from the order of a few nanometres [7]. Based upon this work, it is expected that irrespective of the variation in imaging conditions the strains observed on fused silica are representative of only the top few nanometres of surface induced strains.

The source of the backscattered electron contrast is currently unknown. The contrast zones detected here are unusual, as BSE image contrast should show dependence only on the mean atomic number (Z) of the sample [1, 2]. While indentation of silica has been shown to be accompanied by density increases of silica as high as 15% [13, 19], BSE material contrast is not dependent upon sample density [17], as is illustrated by the identical backscattered electron coefficient, η, found in the polymorphs of carbon - graphite and diamond [20]. Hence, an increase in density cannot be

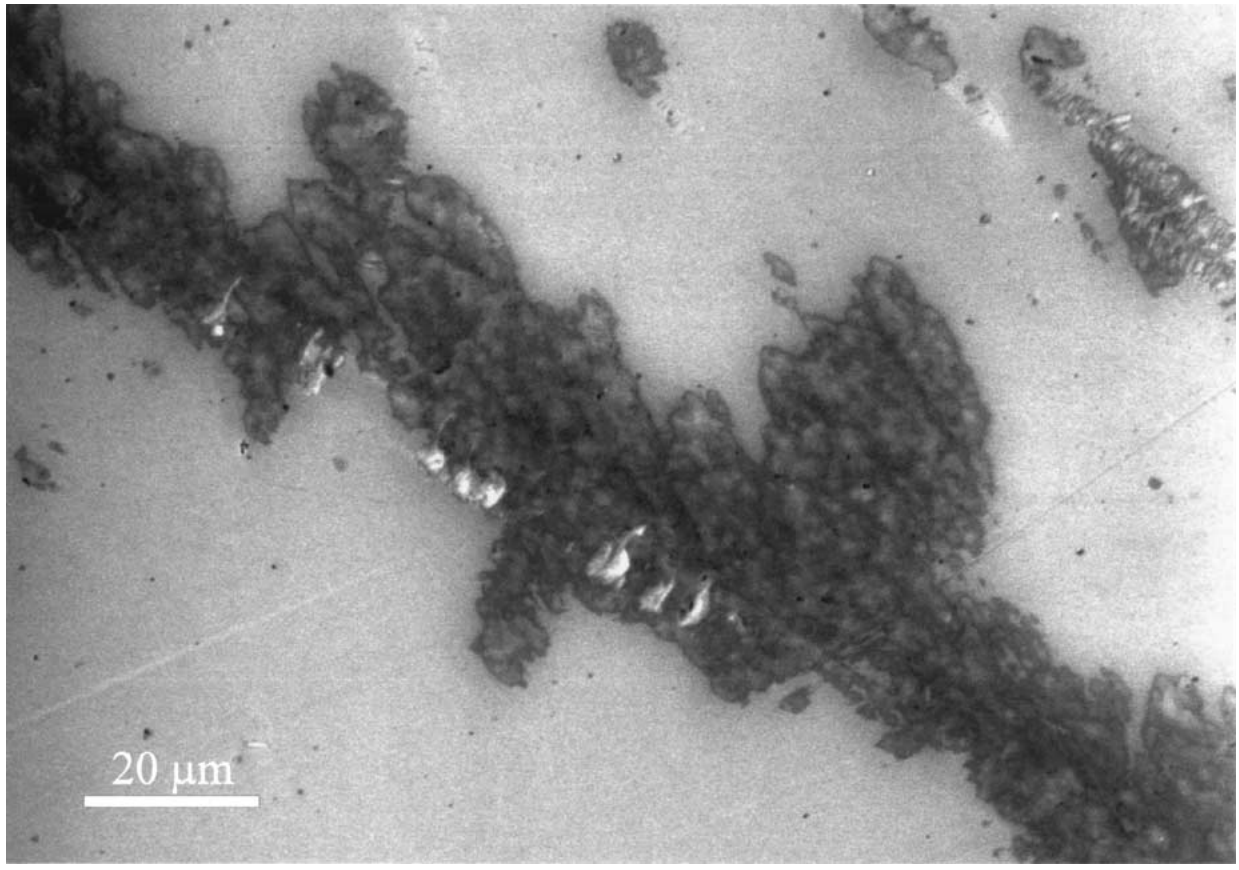

(a)

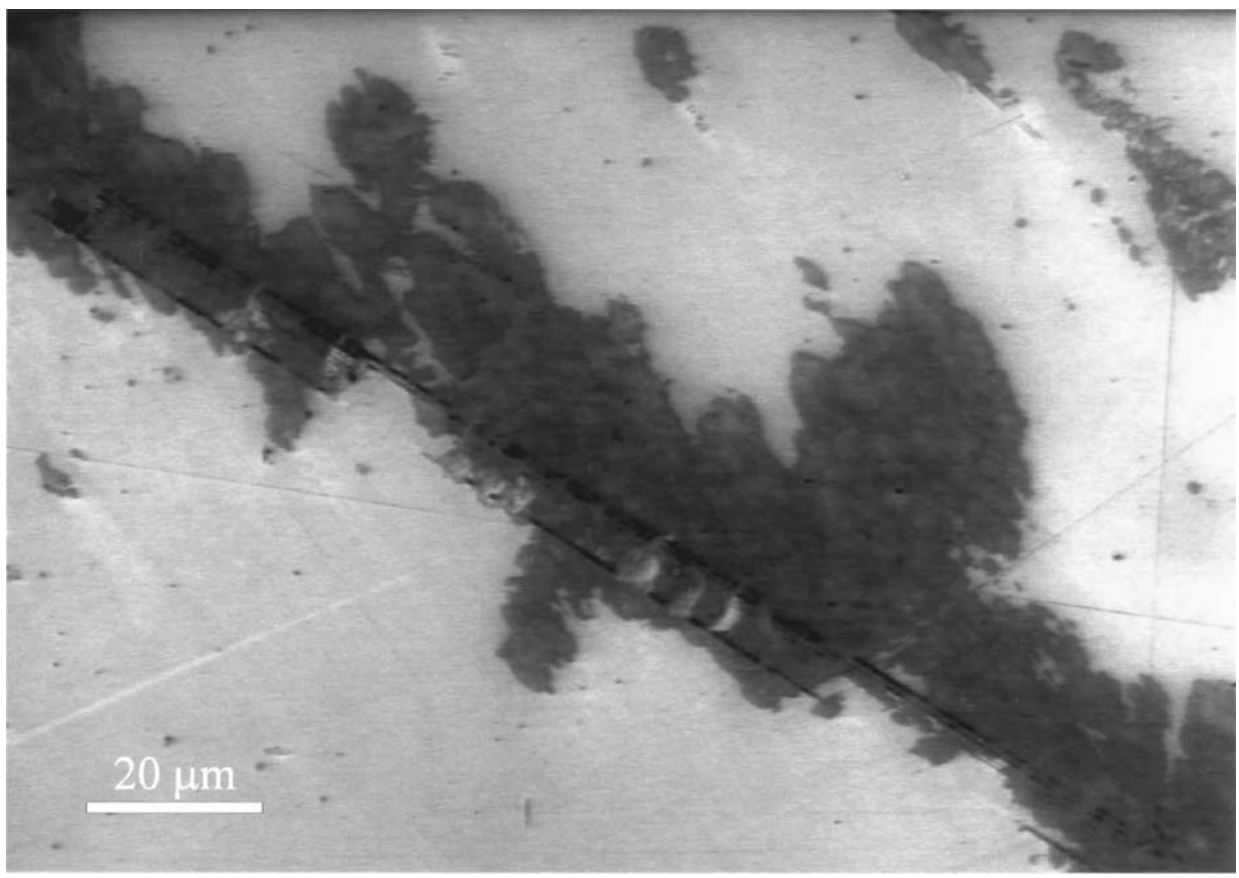

(b)

Figure 5 (a) A CCI image of chemically adhered ceria on fused silica imaged in the FEI XL30 ESEM. Note the contrast between newly adhered ceria (bright particles) and pre-existing adhered ceria. This is due to the influence of a thin silica overlayer ($E = 30$ kV, spot size $= 5$, $P = 0.3$ Torr, WD $= 6.3$ mm). (b) A charge contrast image showing how CCI can be used to detect linear strain defects residing below a layer of adhered ceria approximately 300 nm thick. Ceria powder was found to deposit preferentially over linear defects, some of which extended several millimetres across the sample.

the cause of the BSE contrast observed. Also, analysis using energy dispersive spectrometry (SEM-EDS) reported identical chemical compositions in both deformed and undeformed regions, so Z dependence is also ruled out. As BSE contrast is only observed when using detectors sensitive to lower energy BSE's (ESEM vs. Jeol 6400) [14], this suggests that the component of the electron spectrum responsible for these observations may reside in the low-energy BSE region. Further work is necessary to establish this conclusively.

3.2. Application of CCI to the study of polished glass surfaces

3.2.1. Surface contamination by adhered polishing abrasive

Chemically irreversible adhesion of a cerium dioxide polishing powder (Seimi ceria) was observed during some polishing tests with fused silica. The residue, as measured by AFM, consisted of predominantly linear deposits of ceria approximately 300 nm thick, often extending continuously for several millimetres across the sample or in smaller discrete patches. Fig. 5a shows an ESEM image of these deposits, obtained at low pressure imaging conditions on an uncoated sample in the Electroscan ESEM. Little contrast between the adhered ceria and the surrounding silica substrate is observed, indicating that the CCI condition is sensitive to a thin deposit of silica over the ceria. Confirmation of this was made by comparison with BSE images which showed near identical contrast. Furthermore the silica overlayer was independently confirmed by transmission electron microscopy on particles scraped from the silica surface using energy dispersive x-ray spectrometry (TEM-EDS). A few uncoated ceria particles (bright particles) are recent additions to the deposited layer and exhibit a secondary electron emission more consistent with high atomic number metal oxide SEII emissions. Both SE and BSE images obtained at low pressure conditions in the ESEM appear to have enhanced sensitivity to surface layers, such as the silica layers described.

Fig. 5b shows the identical region to Fig. 5a, under enhanced CCI conditions. Linear defects residing below the 300 nm ceria layer are now observed; a result of the unique sensitivity of this technique to strain detection in fused silica. At the same time, surface scratch defects in uncovered sites also have become apparent. Analysis using AFM, in areas where the defects

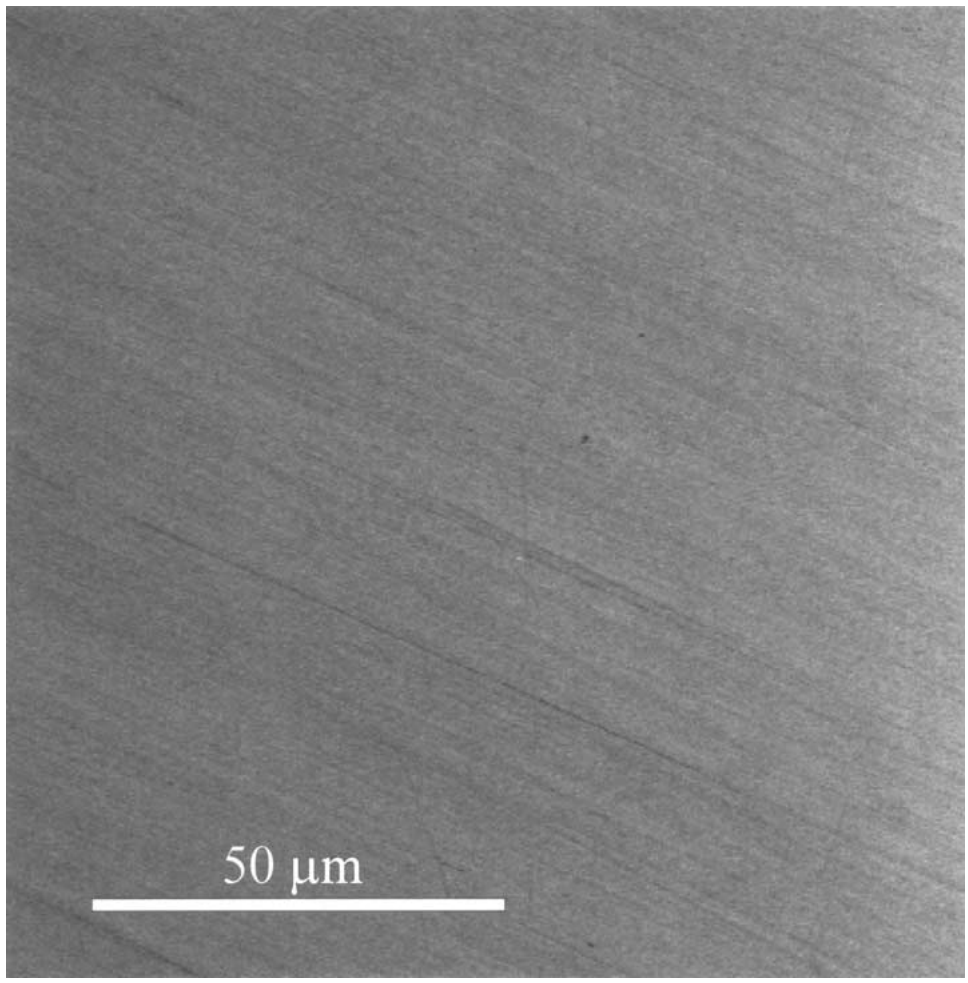

(a)

Figure 6 (a) A CCI image of fused silica polished with Ferro 424-K ceria showing directional strain introduced during polishing, and (b) a 13.5 μm AFM image (2 : 1) of the same sample showing that the CCI contrasts are associated with surface deformation generated by the contact of the polishing particle crystallites with the glass surface during polishing. A roughness line section is provided for comparison (the section orientation is indicated in the image) (*Continued*).

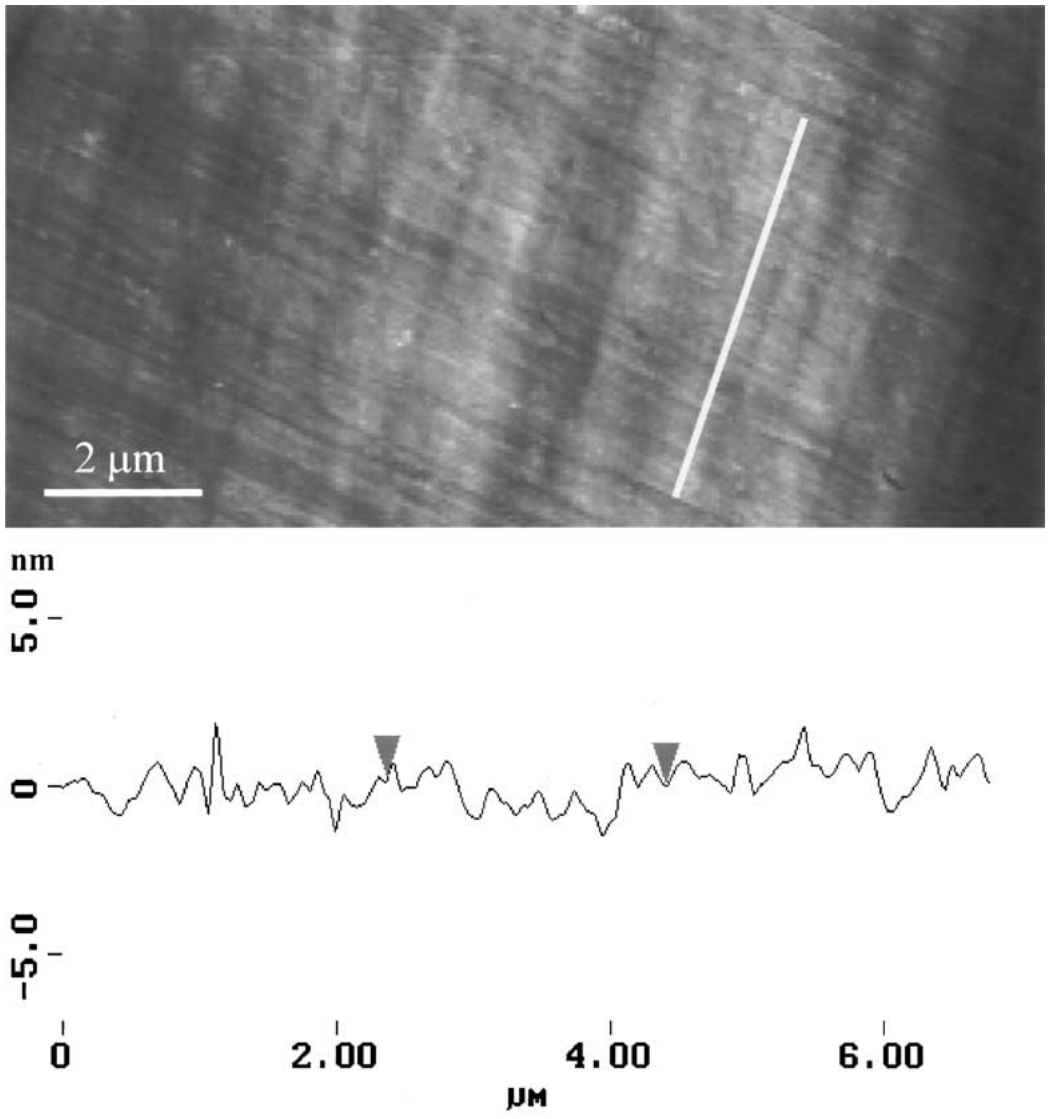

(b)

Figure 6 (*Continued*)

had become uncovered, confirms that they comprise scratches typically 5–30 nanometres deep and up to a micron in width. Despite the sensitivity of FESEM to fine surface detail, analysis of these samples using FESEM showed no indications of underlying defects. Applying CCI across the sample, we have observed a strong tendency for powder to deposit preferentially over defect sites compared with strain free material. Furthermore, deposits tend to orient along these defects, as in Fig. 5b, suggesting some chemical affinity between the polishing powder and strained silica sites. Chemical activity of glass polishing compounds has long been suspected [21] and is the basis for the chemo-mechanical theory of polishing.

3.2.2. Evidence of plastic deformation at the nanometre level

Fig. 6a shows a CCI image of a fused silica sample polished using a commercial cerium dioxide abrasive. Highly directional, homogeneously distributed strain information is noted, with individual resolvable features spatially distributed by approximately 100 nm. No features could be observed using BSE imaging. At higher levels of magnification CCI contrasts were lost due to beam saturation in the sample. This, therefore represents the practical limit of lateral resolution in the CCI technique for this material under these conditions.

Fig. 6b shows an AFM image of the sample with identical sample orientation used during the collection of Fig. 6a. The sample exhibits a surface roughness of 0.9 nm rms measured over a 3.5 micron cut-off length, with peak to valley displacements between adjacent micro-ploughing defects of around 1 nm. There is clearly strong correspondence between features in the CCI and AFM images, and this suggests that the observed CCI contrasts are attributable to residual surface strains resulting from the two body abrasive wear action of the polishing particles, which facilitates densification of the near-surface region in the glass.

In comparison, Fig. 7 shows a CCI image of fused silica sample, polished using an alumina abrasive under identical conditions (pH, solids loading, pressure etc.)

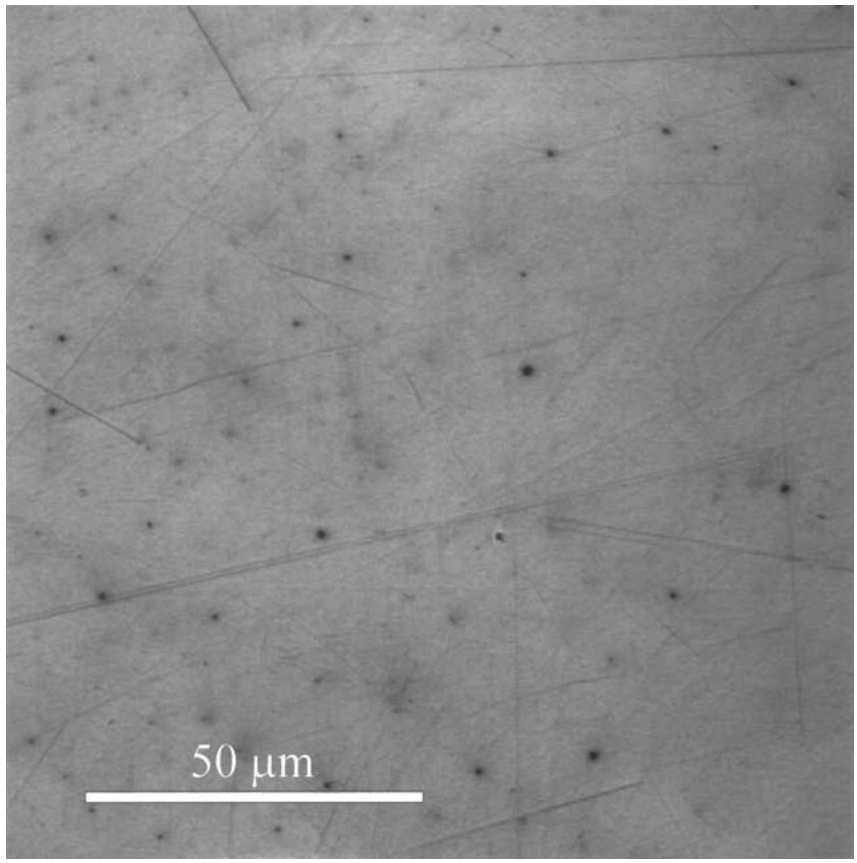

Figure 7 A CCI image of fused silica polished with Ferro Alox alumina power. CCI contrasts of embedment defects and scratches are apparent but there is no indication of directional polishing induced strain as in Fig. 6a.

and with similar particle size distribution and crystallite size ($\sim$2 μm and 60 nm respectively) as the cerium dioxide used to generate the surface in Fig. 6. Defects arising from the intermittent rolling and embedment of the alumina in the silica surface during particle instabilities on the polishing lap are observed. While some scratches are also evident, CCI conditions failed to reveal similar homogeneously distributed lineations as observed on the cerium dioxide polished fused silica, suggesting that the bulk of abrasive contacts do not, in general, lead to densification. This is further supported by an accompanying low surface roughness value of 0.45 nm rms, measured in areas devoid of embedment defects. Under these conditions, specific wear rates of fused silica using the alumina abrasive were measured to be an order of magnitude lower than for the cerium dioxide abrasive, despite identical polishing conditions, with alumina and cerium dioxide rates measured as 3.8×10^{-14} Pa^{-1} and 4.62×10^{-13} Pa^{-1} respectively.

The visualisation of surface induced strain accompanying the cerium dioxide polished sample is suggestive that the polishing process can generate sufficient mechanical stresses to yield and densify surface layers. This observation is consistent with previous ellipsometric [22, 23] and X-ray relectivity [24] measurements of polish induced changes in surface refractive indicies of fused silica glass. Comparison of imaged surface strains and measured wear rates suggests that glass removal during polishing may be facilitated by surface densification, perhaps through strain activated hydrolytic weakening of the silica network [25, 26] facilitating material removal though mechanical abrasion or dissolution.

4. Conclusion

A recently developed application of ESEM known as charge contrast imaging has been described, which enables the imaging of near surface strains in fused silica glass using environmental scanning electron microscopes utilising gaseous secondary electron detectors. We have shown the suitability of CCI in visualising surface deformations introduced into glass by techniques such as indentation. Complementing this technique, we have also shown subtly different strain information can also be observed by using backscattered electron detection, though this technique appears not to be as surface specific as charge contrast imaging. The source of the electron signals giving rise to these effects are currently unknown.

Application of CCI to the study of polishing in glasses has provided qualitative evidence of the chemical nature of polishing compounds in preferentially selecting defect sites on the glass surface to chemically bond with. Contrasts observed on finely polished glass surface have also provided supporting evidence for densification processes induced by the passage of polishing particles over the glass surface.

Acknowledgements

The authors would like to extend their thanks to Brian Lawn of NIST and David Joy of ORNL for constructive

discussions. Thanks to Roz Wealthall for her assistance with imaging. One of the authors (SPG) would like to acknowledge the assistance of the Materials Institute of Western Australia, Ashton Lanthanides NL. and a University Postgraduate Award for contributing support. BJG gratefully acknowledges an Australian Research Council SPIRT grant and support from Alcoa World Alumina.

References

1. J. I. GOLDSTEIN, D. E. NEWBURY, P. ECHLIN, D. C. JOY, C. FIORI and E. LIFSHIN, "Scanning Electron Microscopy and X-Ray Analysis" (Plenum Press, New York, 1981).
2. D. E. NEWBURY, D. C. JOY, P. ECHLIN, C. FIORI and J. I. GOLDSTEIN, "Advanced Scanning Electron Microscopy and X-Ray Microanalysis" (Plenum Press, New York, 1986).
3. M. POSTEK and C. J. EVANS, *Scanning Microscopy* **3** (1989) 435.
4. T. SUGANUMA, *Journal of Electron Microscopy* **34** (1985) 328.
5. B. J. GRIFFIN, *Microscopy and Microanalysis* **3** (1997) 1197.
6. *Idem*., *Scanning* **22** (2000) 234.
7. D. DROUIN and B. J. GRIFFIN, in Proceedings of the WASEM & AXAA Conference, Mandurah, Western Australia, 1998, edited by B. J. Griffin (Western Australian Society for Electron Microscopy, Western Australia) p. 69.
8. G. D. DANILATOS, *Advances in Electronics and Electron Physics* **71** (1998) 109.
9. T. C. BARONI, B. J. GRIFFIN, J. R. BROWNE and F. J. LINCOLN, *Microscopy and Microanalysis* **6** (2000) 49.
10. B. J. GRIFFIN, A. VAN RIESSEN and L. M. EGERTON-WARBURTON, *Scanning* **17** (1995) V58.
11. R. F. COOK and G. M. PHARR, *J. Amer. Ceram. Soc*. **73** (1990) 787.
12. J. D. MACKENZIE, *ibid*. **46** (1963) 461.
13. C. R. KURKJIAN and G. W. KAMMLOTT, *ibid*. **78** (1995) 737.
14. G. D. DANILATOS, *Scanning Microscopy Supplement* **7** (1993) 57.
15. M. TOMOZAWA, K. YANG, H. LI and S. P. MURARKA, in Materials Research Society Symposium Proceedings, 1994 (Materials Research Society) p. 89.
16. J. S. TSE, D. D. KLUG and D. LEPAGE, *Phys. Rev. B* **46** (1992) 5933.
17. D. C. JOY, "Monte Carlos Modelling for Electron Microscopy and Microanalysis" (Oxford University Press, New York, 1995).
18. B. J. GRIFFIN, in Proceedings of the WASAM/AXAA Joint Conference, Mandurah, Western Australia, September 26–27 1998, edited by B. J. Griffin, A. van Riessen (Western Australian Society for Electron Microscopy, Western Australia) p. 79.
19. R. J. HEMLEY, C. T. PREWITT and K. J. KINGMA, "Reviews in Mineralogy—Silica: Physical Behaviour, Geochemistry, and Materials Applications" Vol. 29 (Mineralogical Society of America, Washington D.C., 1994) p. 41.
20. D. C. JOY, "A Database of Electron-Solid Interactions" (EM Facility, University of Tennessee, 2001).
21. L. M. COOK, *J. Non-Cryst. Solids* **120** (1990) 152.
22. M. MALIN and K. VEDAM, *J. Appl. Phys*. **48** (1977) 1155.
23. H. YOKOTA, H. SAKATA, M. NISHIBORI and K. KINOSITA, *Surf. Sci*. **16** (1969) 265.
24. W. E. WALLACE, W. L. WU and R. A. CARPIO, *Thin Solid Films* **280** (1996) 37.
25. T. A. MICHALSKE and S. W. FREIMAN, *Nature* **295** (1982) 511.
26. M. TOMOZAWA, *Solid State Tech*. July (1997) 169.

Received 22 June 2000
and accepted 3 August 2001